Journal of Power Sources 197 (2012) 20–27

Contents lists available at SciVerse ScienceDirect

Journal of Power Sources

journal homepage: www.elsevier.com/locate/jpowsour

Surface and interface behaviors of Sr-doped lanthanum manganite air electrode in different moisture atmospheres

Tongan Jin, Kathy Lu*

Department of Materials Science and Engineering, Virginia Tech, Blacksburg, Virginia 24061, USA

ARTICLE INFO

Article history:
Received 7 July 2011
Received in revised form 29 August 2011
Accepted 9 September 2011
Available online 16 September 2011

Keywords:
Solid oxide fuel/electrolyzer cell
Air electrode
Sr-doped lanthanum manganite
Moisture
Diffusion

ABSTRACT

Surface and interface reactions of the air electrode with the contacting components of solid oxide cells are essential for the long term operation stability and performance. In this work, an yttria-stabilized zirconia electrolyte (YSZ)/strontium-doped lanthanum manganite electrode (LSM)/AISI 441 alloy interconnect tri-layer structure has been fabricated in order to simulate the working environment of a real cell with Cr-containing interconnect. The samples are thermally treated in moist air atmospheres (0 vol%, 10 vol%, and 25 vol% moisture) at 800 °C for up to 500 h. The interactions among different cell components are characterized. The LSM air electrode shows slight grain growth but the growth is less in moist atmospheres. High moisture level affects the bonding between the LSM and the YSZ and leads to the formation of small particles on the YSZ surface. The amount of Cr deposition on the LSM surface is slightly more for the samples thermally treated in the moist atmospheres and shows no significant difference between the 10 vol% and 25 vol% moisture air. At the YSZ/LSM interface, La enrichment is significant and facilitates the Cr deposition while Mn depletion occurs. The YSZ surface composition is not strongly affected by the atmosphere.

1. Introduction

Solid oxide cells (SOCs), including solid oxide fuel cells (SOFCs) and solid oxide electrolyzer cells (SOECs), are promising electrochemical devices that generate electricity from fuel or produce hydrogen by splitting water. In order to obtain desired power output or hydrogen production, SOC stacks of planar geometry are widely investigated [1–5].

Ferritic stainless steel with a high Cr content has been intensively studied as a cost effective interconnect material for SOC stacks working at 700–900 °C [6–8]. Perovskite materials have been widely investigated as air electrode materials, such as Sr-doped lanthanum manganite (LSM) and Sr-doped lanthanum ferrite [9–11]. The air electrode is fabricated on the electrolyte, such as yttria-stabilized zirconia (YSZ), to reduce the oxygen molecules into oxygen ions (in the SOFC mode) or to oxidize the oxygen ions to oxygen molecules (in the SOEC mode):

$$\text{SOFC}: 1/2O_2(\text{gas}) + 2e^-(\text{cathode}) \rightarrow O^{2-} \quad (1)$$

$$\text{SOEC}: O^{2-}(\text{electrolyte}) \rightarrow 1/2O_2(\text{gas}) + 2e^- \quad (2)$$

The ceramic air electrode of SOCs sintered with the electrolyte should have certain porosity and thickness in order to provide gas flow route and active sites for the above electrochemical reactions. At the contact between the electrolyte and the air electrode, the triple phase boundary (TPB) is the active area for the oxygen reduction/oxidation reactions, which is essential to the cell performance and determined by the microstructure of the electrolyte/air electrode interface [12]. For the long term operation, the air electrode should be stable in the high temperature oxidizing environment and chemically compatible with other contacting cell components [13,14]. Undesirable interactions can cause the degradation of the cell stacks. For the air electrode, grain size and porosity as well as TPB structure influence the cell performance [15–17]. Foreign phases formed at the interface due to the solid state reactions can also affect the active sites. For example, $La_2Zr_2O_7$ and $SrZrO_3$ formed at the YSZ/LSM interface block the TPBs and cause an increase in the ohmic resistance [18–20]. Furthermore, the deposition of poisoning species such as Cr species from the ferritic stainless steel across the air electrode and at the TPBs is a critical issue in cell degradation [21–25].

The degradation of the air electrode caused by the Cr-containing alloy interconnects (chromium poisoning) [26,27] includes three steps: oxidation and vaporization of Cr species from the surface of the interconnect, the diffusion of the Cr species, and the interaction between the vapor phase Cr species and the air electrode. Formation of the vapor phase Cr species is believed to be strongly

* Corresponding author. Tel.: +1 540 231 3225; fax: +1 540 231 8919.
E-mail address: klu@vt.edu (K. Lu).

0378-7753/$ – see front matter © 2011 Elsevier B.V. All rights reserved.
doi:10.1016/j.jpowsour.2011.09.022

Table 1
Nominal composition of AISI 441 alloy (wt%) [32,34].

Cr	Fe	Mn	Ti	Si	Al	C	S	P	Ni	Nb	Re
17.6	80.68	0.33	0.18	0.47	0.045	0.01	0.001	0.024	0.20	0.46	-

dependent on the atmosphere. CrO_3 and $CrO_2(OH)_2$ are the two major compounds of the volatile Cr species, and $CrO_2(OH)_2$ is the dominant phase when water vapor is present in the atmosphere [28,29].

$$Cr_2O_3 + 3/2O_2 \rightarrow 2CrO_3 \quad (3)$$

$$Cr_2O_3 + 3/2O_2 + 2H_2O \rightarrow 2CrO_2(OH)_2 \quad (4)$$

Besides that the volatile Cr species are strongly affected by the water vapor in the atmosphere, Nielsen et al. observed that the SOFC voltage dropped 70% in 12.8 mol% moisture air and small particles appear on the YSZ surface [30]. Kim et al. observed ~25% cell voltage drop when using a 40 vol% moisture content. Composition analysis showed that La_2O_3 forms on the LSM air electrode surface and decreases conductivity [31].

AISI 441 is a promising stainless steel interconnect material that shows good stability in the SOFC working environment, forms a $(Mn,Cr)_3O_4$ layer, and decreases the Cr evaporation [32,33]. The composition of the alloy is shown in Table 1. As seen, AISI 441 has a high content of Fe (80.7 wt%) followed by Cr (17.6 wt%). However, the stability of AISI 441 with the air electrode in high moisture atmosphere has not been reported.

In order to improve the understanding of the Cr species interaction with the air electrode, different moisture atmospheres are introduced in this study through the electrolyte/air electrode/interconnect tri-layer configuration (8% yttria-stabilized zirconia (YSZ)/$La_{0.8}Sr_{0.2}MnO_3$ (LSM)/AISI 441). The samples are thermally treated at 800 °C for up to 500 h in dry air, 10 vol% moisture air, and 25 vol% moisture air, respectively. Scanning electron microscopy (SEM) is used to characterize the morphology changes of the LSM porous air electrode and the YSZ/LSM interface. X-ray photoelectron spectroscopy (XPS) is used to obtain surface chemistry and elemental distribution across the LSM layer. X-ray diffraction (XRD) and energy dispersive spectroscopy (EDS) are used to investigate the Cr deposition difference in the different atmospheres.

2. Experimental procedures

2.1. Sample preparation

LSM powder was prepared by conventional solid state reaction method [35]. AISI 441 ferritic stainless steel samples (ATI Allegheny Ludlum Corporation, Brackenridge, PA) were prepared as rectangular substrates (25.4 mm × 25.4 mm, thickness 2.08 mm). They were polished to optical finish to remove the oxidized layer, if any, and to obtain a scratch free flat surface. The polished samples were cleaned by ultrasound in water first and then in acetone.

The LSM air electrode was fabricated on the YSZ surface by screen printing [36]. The LSM layer on the YSZ substrates (20 mm diameter, 250–290 μm thickness, Nextech Materials, Lewis Center, OH) was 20–30 μm thick after being sintered at 1100 °C for 2 h. After the sintering of the YSZ/LSM bi-layer, the AISI 441 alloy was placed on the LSM electrode side as the interconnect. The details of the tri-layer sample configuration can be found in the previous work [37].

Thermal treatment was carried out in dry air (compressed air), 10 vol% and 25 vol% moisture air at 800 °C for 500 h. The thermal treatment set-up was given before [37]. The flow rates were 10 ml s^{-1} for the dry air, 10 ml s^{-1} air/1.1 ml s^{-1} water vapor for the 10 vol% moisture air, and 30 ml s^{-1} air/10 ml s^{-1} water vapor for the 25 vol% moisture air respectively.

2.2. Characterization

After the thermal treatment, the tri-layer samples were broken to examine the cross-sections. SEM (Quanta 600 FEG, FEI, Hillsboro, OR) was used to study the microstructure. The EDS module (Bruker AXS, MiKroanalysis Gmbh, Berlin, Germany) attached to the SEM was used for compositional spot analysis. Some samples were mounted into epoxy, and then cut and ground to detect different positions (distances away from the AISI 441 layer) in the porous LSM air electrode by an X-ray photoelectron spectrometer (XPS, PHI Quantera SXM-03, Physical Electronics Inc., Chanhassen, MN). An Al Kα radiation (1486.6 eV) was used as the X-ray source. Along the 30 μm thick LSM layer, the examined locations were shown in Fig. 1. They were labeled as YSZ/LSM, LSM Left, LSM Middle, LSM Right, and LSM/AISI 441 from the YSZ to the AISI 441. In order to identify the phases, X-ray diffraction (XRD) studies were carried out in an X'Pert PRO diffractometer (PANalytical B.V., EA Almelo, The Netherlands). The step size was 0.030 s^{-1} with Cu Kα radiation (λ = 1.5406 Å).

3. Results

3.1. Microstructure

Fig. 2(a) shows the microstructure of the LSM layer at the LSM/AISI 441 interface before and after the thermal treatment in the different atmospheres. The AISI 441 interconnect was removed after the thermal treatment; the SEM images in Fig. 2(a) are taken at the LSM "top" surface, which is directly in contact with the AISI 441 polished surface. Before the thermal treatment, the microstructure of the porous LSM layer shows grain sizes around 3 μm (Fig. 2(a)). After the thermal treatment in dry air for 500 h, the grains grow larger, whereas some small grains adhere together and form large grains of about 5 μm size. Also, the grains become more roundish compared with those before the thermal treatment. The air

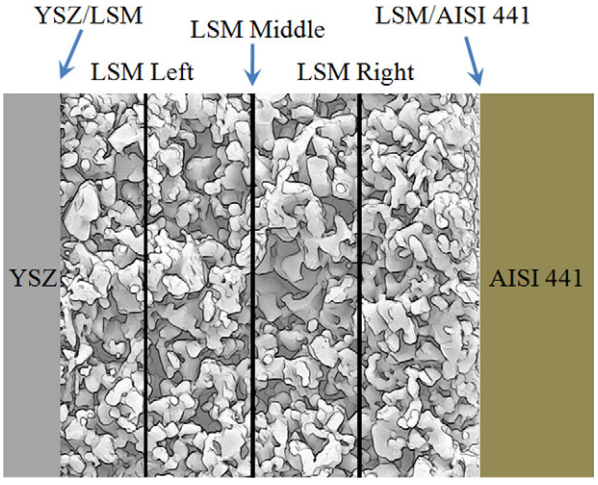

Fig. 1. The examination locations of the porous LSM air electrode. XPS is carried out at five locations: YSZ/LSM, LSM Left, LSM Middle, LSM Right, and LSM/AISI 441.

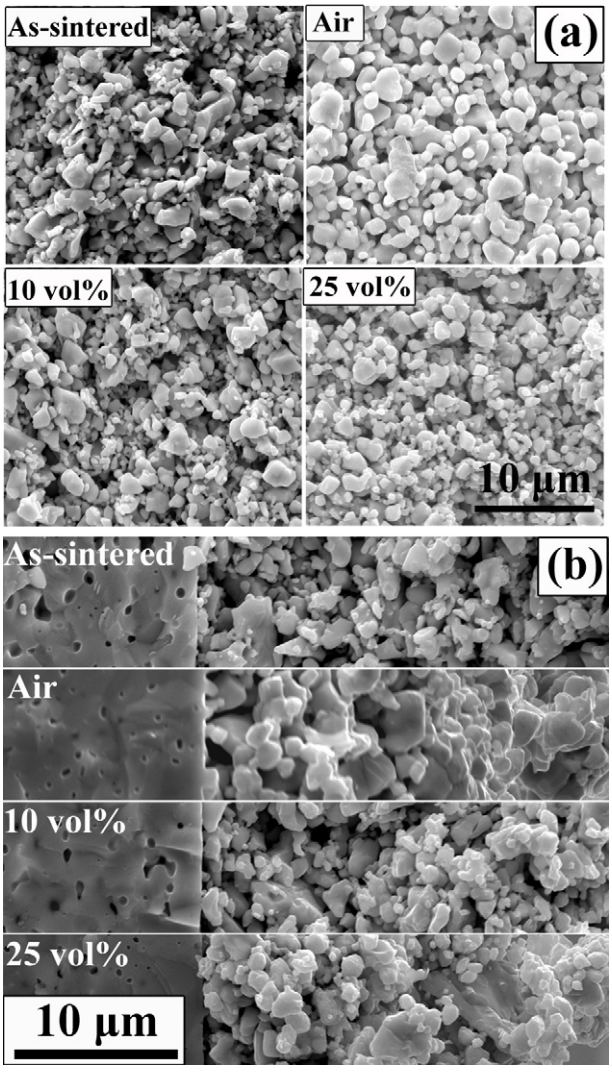

Fig. 2. SEM images of the LSM porous layer before and after the thermal treatment in the different moisture atmospheres at 800 °C for 500 h: (a) the LSM side in contact with the AISI 441 interconnect, (b) fractured cross section, the dense YSZ electrolyte is on the left.

electrode looks dense. For the samples thermally treated in 10 vol% and 25 vol% moisture atmospheres, the microstructures are almost the same, with the latter having more roundish grains. The grain growth and morphology change are both relatively less than those of the dry air treated sample. Based on this observation, it can be concluded that dry air induces more sintering than moist atmospheres during the thermal treatment.

The cross sections of the LSM layer and the YSZ/LSM interface are shown in Fig. 2(b). The YSZ/LSM samples were fractured to obtain the cross sections and avoid morphological alteration from polishing. The LSM air electrode layer shows good adhesion with the YSZ electrolyte after sintering and after the thermal treatment. No visible cracks in the porous air electrode or at the interface are observed. The microstructure of the LSM porous air electrode is homogeneous across the LSM thickness, where no differences are seen from the left (YSZ/LSM interface) to the right (LSM/AISI 441 interface). The microstructure of each sample is consistent with the LSM "top" surface. The sample thermally treated in dry air shows the most significant grain growth among all the samples, where small grains adhere together and form large grains over 5 μm size. For the samples thermally treated in 10 vol% and 25 vol% moisture air, the grain growth and bonding are observed but less than those for the dry air treated sample. The 25% moisture sample shows more sintering than the 10 vol% moisture sample.

The YSZ/LSM interfacial behaviors of the thermally treated samples are also examined (Fig. 3). Fig. 3(a) is the original surface of the YSZ substrate (without any LSM layer) after sintering, which shows clear grain boundaries. Fig. 3(b–e) are the SEM images taken from the YSZ surface after the LSM layer being mechanically peeled off. In order to preserve the morphologies at the interfaces, the LSM layers were carefully scratched off and no further disturbance was involved. Bonding spots and some remaining LSM grains can be seen on the YSZ surface. For the YSZ/LSM interface after sintering, small contact spots with mostly less than 500 nm sizes are observed on the YSZ surface (Fig. 3(b), pointed by the arrows). The YSZ grain boundaries are still visible. After the thermal treatment at 800 °C for 500 h in dry air (Fig. 3(c)), the bonding spots substantially increase and the spot size increases to ~1 μm (pointed by the arrows). No YSZ grain boundaries can be seen. This means more extensive contacts are formed during the thermal treatment. This result is consistent with the microstructure of the LSM layer (Fig. 2(b)). The bonding spots for the sample thermally treated in dry air, however, are clean. For the sample thermally treated in 10 vol% moisture air (Fig. 3(d)), individual bonding spots are flatter but harder to distinguish. On the YSZ surface, the grain boundaries are hard to be seen and many small particles with less than 50 nm size are observed. These small particles tend to distribute along the boundaries of the YSZ grains. For the sample thermally treated in 25 vol% moisture air, the bonding merges into a continuous layer and the YSZ grain boundaries are invisible (Fig. 3(e)). More small particles are seen with larger sizes (~100 nm) and more scattering over the interface.

EDS spot analysis is used to determine the composition of the YSZ surface after the LSM layer removal (Fig. 4). The examination locations are marked as "+" in Fig. 3. The results show that the main elements are Zr and Y (the peaks are very strong and not shown in Fig. 4). This is expected because of the presence of the YSZ substrate. The minor elements are La and Mn (approximately less than 1 at%), which means the analyzed spots contain small amounts of La and Mn. Cr deposition on the surface is of a very small amount and the main EDS peak $Cr_{K\alpha}$ overlaps with $La_{L\beta2}$, one of the minor peaks of La; and $Mn_{K\alpha}$, the main peak of Mn, overlaps with a minor Cr peak $Cr_{K\beta}$ [37]. Since La shows relatively strong peaks, for comparison purpose, the $La_{L\alpha}$ peak is used as a reference to compare other elements. Fig. 4 is rescaled to obtain approximately the same intensity for the $La_{L\alpha}$ peaks. The as-sintered sample shows a very small $Mn_{K\alpha}/Cr_{K\beta}$ peak. After the thermal treatment, the peak height increases for all the samples. However, the $Mn_{K\alpha}/Cr_{K\beta}$ peak increases the most for the sample thermally treated in dry air and the least for the samples thermally treated in the 25 vol% moisture air. Compared with the main $La_{L\alpha}$ peak, the $Cr_{K\alpha}/La_{L\beta2}$ peak shows no significant difference between the as-sintered state (no Cr deposition) and the thermally treated samples (with Cr deposition), which means the $Cr_{K\alpha}$ peak is very weak. From this, it can be deduced that the contribution of the $Cr_{K\beta}$ peak is very weak and the $Mn_{K\alpha}/Cr_{K\beta}$ peak intensity represents the Mn content. This result means that Mn deposits relatively less in the high moisture atmosphere.

3.2. Deposition and distribution of different species

After the thermal treatment at 800 °C for 500 h in different atmospheres, the AISI 441 interconnects were removed and XPS analysis was carried out at different locations across the LSM layer. A detailed XPS experimental description can be found in the previous work [37]. Along the porous LSM air electrode layer (~30 μm thick), five different locations are obtained for the XPS analysis (Fig. 5). The thickness of each layer is controlled by a

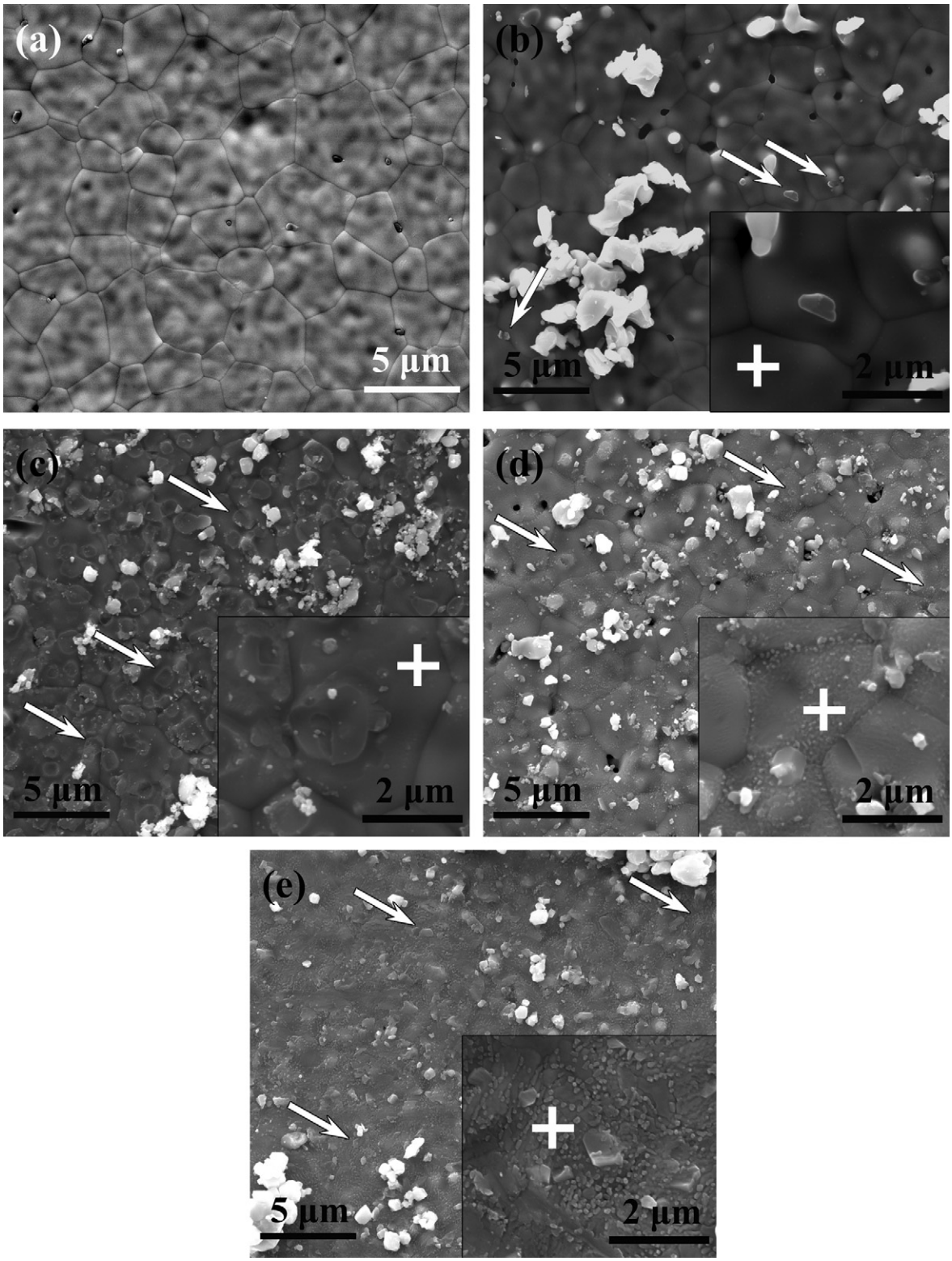

Fig. 3. SEM images of the YSZ/LSM interface after the LSM porous layer removal: (a) YSZ surface, (b) as-sintered, (c) thermally treated in dry air, (d) thermally treated in 10 vol% moisture air, and (e) thermally treated in 25 vol% moisture air.

micrometer at ~8 μm. The results are normalized to 100% by considering La, Sr, Mn, and Cr only in order to avoid errors by oxygen from the mounting epoxy. The elemental concentrations are averaged by three measurements at each location.

The surface compositions of the LSM "top" layer after sintering at 1100 °C for 2 h (shown in Fig. 2(a), "As-sintered") show significant enrichments of La and Sr (not shown in Fig. 5(a–c)). The contents of La, Sr, and Mn are 49.6%, 14.3%, and 36.1%, which are very different from the designed 40% La, 10% Sr, and 50% Mn (it should be mentioned that all the elemental analysis data in this paper are presented in atomic percent). La and Sr increase by 24% and 42%, respectively, and Mn decreases by 28%. This means the

surface composition has changed after sintering, where Sr enriches the most, La enriches less than Sr, and Mn content depletes accordingly at the LSM surface. Such Sr and La surface segregation and Mn depletion have been observed before, and are believed to result from the strain energy driven re-distribution of the ions [37].

After the thermal treatment in dry air, at the LSM/AISI 441 interface, the contents of La, Sr, Mn, and Cr are 45.0 ± 1.0%, 15.6 ± 0.3%, 30.7 ± 0.3%, and 8.7 ± 1.3%, respectively. The surface composition is very close to that of the as-sintered state if Cr is excluded. In the 10 vol% moisture air, the contents of La, Sr, Mn, and Cr are 50.6 ± 1.5%, 12.3 ± 1.2%, 27.9 ± 0.5%, and 9.2 ± 0.2%, respectively. In the 25 vol% moisture air, the contents are 50.3 ± 0.7%, 14.3 ± 0.5%, 24.4 ± 1.1%, and 11.1 ± 1.5%, respectively. This indicates that the thermal treatment leads to Cr deposition. As the moisture content increases, La enrichment increases, Sr enrichment decreases, and Mn depletion worsens. For the samples treated in the 10 vol% and 25 vol% moisture air, La surface enrichment is ~10% higher than that for the dry air treated sample. At the same time, Cr deposition increases monotonically with the water content, from 8.7% to 9.2%, and to 11.1%, which is a considerable amount and reflects the Cr deposition on the air electrode.

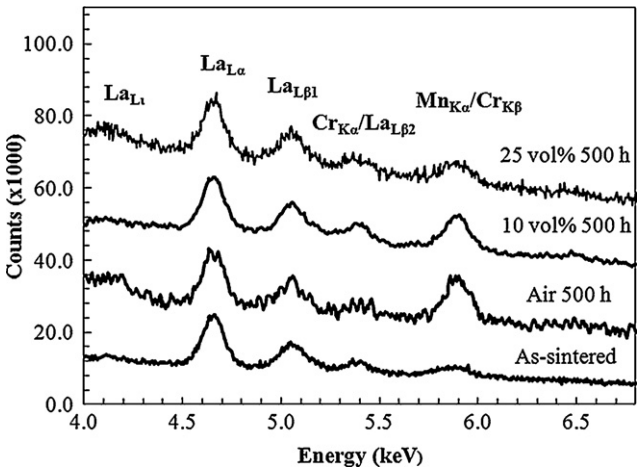

Fig. 4. EDS spot analysis of YSZ/LSM interface after the LSM porous layer removal. The analyzed spots are on the YSZ surface. The corresponding locations are shown in Fig. 3(b–e), marked by crosses.

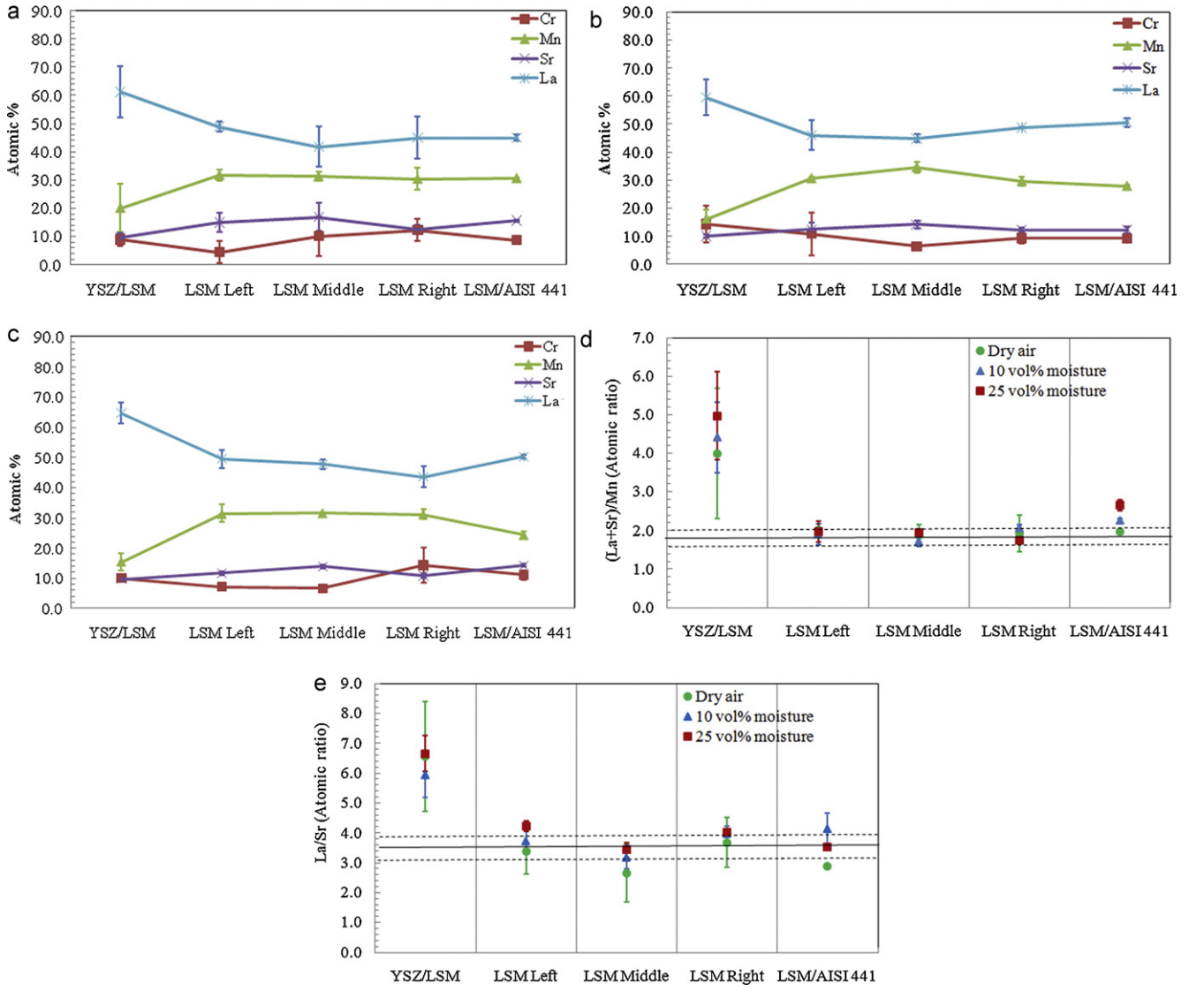

Fig. 5. Composition of the LSM layer before and after the thermal treatment at 800 °C for 500 h in different atmospheres: (a) dry air, (b) 10 vol% moisture air, and (c) 25 vol% moisture air. All the concentrations are normalized to 100% by considering La, Sr, Mn, and Cr only. Atomic ratios: (d) (La + Sr)/Mn ratio, (e) La/Sr ratio. The solid and dash lines mark the values and standard deviations of the ratios before the thermal treatment.

Across the LSM porous layer, the contents of La, Sr, and Mn show different changes from the right to the left of the tri-layer assembly. For the LSM sample thermally treated in dry air, the La, Sr, and Mn contents are almost the same as those at the LSM/AISI 441 interface. For the sample thermally treated in 10 vol% moisture air, the composition is also fairly consistent with some random variations such as the higher Mn content at the LSM Middle location. For the sample thermally treated in 25 vol% moisture air, the contents of La and Sr decrease by about 10% and 20%, respectively, and Mn increases by about 20% at the LSM Right location compared with those at the LSM/AISI 441 interface. These results indicate that higher water vapor content in the atmosphere causes more La and Sr composition segregation at the LSM/AISI 441 interface but the segregation are also limited to the interface.

At the YSZ/LSM interface, much higher La content is detected at 61.3 ± 9.0% in dry air, 59.5 ± 6.3% in 10 vol% moisture air, and 64.8 ± 3.5% in 25 vol% moisture air. On the other hand, the Mn content is lower than those across the LSM layer and at the LSM/AISI 441 interface, which are 20.1 ± 8.4% in dry air, 16.2 ± 3.2% in 10 vol% moisture air, and 15.4 ± 2.7% in 25 vol% moisture air. Sr content also decreases compared with those across the LSM layer at 9.6 ± 1.8% in dry air, 10.0 ± 0.6% in 10 vol% moisture air, and 9.8 ± 0.5% in 25 vol% moisture air, even though they are close for the samples thermally treated in dry and moisture atmospheres. This means La is more favorable to interact with the YSZ electrolyte and likely forms La-containing compounds at the interface. Sr and Mn segregate inwards to the LSM layer. Water vapor in the atmosphere increases the La enrichment and Mn depletion while having negligible effect on the Sr composition at the YSZ/LSM interface.

After the thermal treatment, Cr is detected at all the locations of the tri-layers for all three conditions. At LSM Right (close to the AISI 441), the Cr contents are 12.2 ± 3.9% in dry air, 9.4 ± 2.1% in 10 vol% moisture air, and 14.4 ± 5.9% in 25 vol% moisture air, which are similar to the Cr contents at the LSM/AISI 441 interface and show no clear impact from moisture. The lowest Cr contents of the samples are 4.4 ± 3.9% for LSM Right in dry air, 6.4 ± 1.0% for LSM Middle in 10 vol% moisture air, and 6.6 ± 1.2% for LSM Middle in 25 vol% moisture air, respectively. This means higher moisture leads to higher Cr deposition at the "deeper" locations close to the YSZ, which is probably because of the different concentrations of the volatile Cr species. At the YSZ/LSM interface, the Cr content increases to 9.0 ± 2.5% in dry air, 14.4 ± 8.6% in 10 vol% moisture air, and 10.0 ± 1.7% in 25 vol% moisture air. Still, high moisture content aggravates Cr deposition at the YSZ/LSM interface. For all the thermal treatment conditions, the Cr content first decreases from right to left along the cross section of the LSM layer and then increases, which shows the preferential deposition of Cr at the YSZ/LSM interface, the TPBs. For the samples thermally treated in 10 vol% and 25 vol% moisture air, the Cr content increases at the LSM Left location compared with that of the LSM Middle location. Cr accumulates at the YSZ/LSM interface and shows even higher concentrations, as much as over 50% compared with the lower values at LSM Middle or LSM Left. The higher Cr content at the LSM Left location for the moisture air conditions is a propagation of the high Cr content at the YSZ/LSM interface. This means high water vapor not only accelerates Cr accumulation at the YSZ/LSM interface but also causes a larger extent of Cr deposition in the adjacent region.

The surface composition changes for the thermally treated samples at different conditions can be more clearly seen from the atomic ratios of the involving elements (Figs. 5(d and e)). The solid and dash lines mark the values and standard deviations of the (La + Sr)/Mn and La/Sr ratios of the LSM layer before the thermal treatment. At this condition, the (La + Sr)/Mn ratio is 1.8 ± 0.2, which is much higher than the designed ration of 1.0 and shows the surface enrichment of La and Sr and depletion of Mn; and the La/Sr ratio is 3.5 ± 0.4, which is less than the designed ratio of 4.0

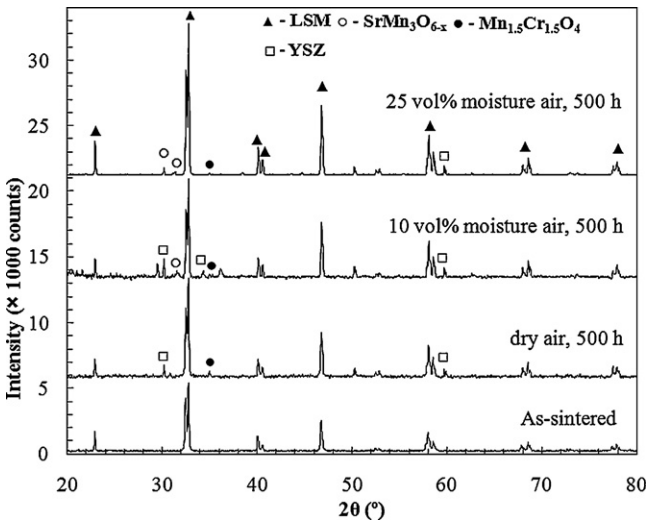

Fig. 6. XRD patterns of the LSM surface in contact with the AISI 441 interconnect before and after the thermal treatment at 800 °C in different atmospheres for 500 h.

and indicates that the Sr surface enrichment is more significant [37]. After the thermal treatment in different atmospheres, these two ratios do not show significant changes across the LSM porous layer (LSM Left, LSM Middle, and LSM Right in Figs. 5(d and e)). These results mean that the composition of the LSM layer does not change significantly during the thermal treatment in the different atmospheres.

At the LSM/AISI 441 interface, the (La + Sr)/Mn ratios are all higher than that of the as-sintered state, and the moist air treated samples show higher values than the dry air treated sample. This means water vapor leads to more La and Sr enrichments on the LSM "top" surface. The chemical composition at the YSZ/LSM interface shows more remarkable enrichment of La (Fig. 5(e)), which is consistent with the microstructure (Fig. 3) and the EDS results (Fig. 4). At the YSZ surface, the (La + Sr)/Mn ratios are 4.0 ± 1.7% in dry air, 4.4 ± 0.9% in 10 vol% moisture air, and 5.0 ± 1.1% in 25 vol% moisture air; the La/Sr ratios are 6.5 ± 1.8% in dry air, 5.9 ± 0.7% in 10 vol% moisture air, and 6.7 ± 0.6% in 25 vol% moisture air. La accumulates and forms new species such as $La_2Zr_2O_7$ with YSZ (Figs. 3 and 4) [18,38].

3.3. LSM/AISI 441 interfacial phase evolution

XRD is used to analyze the phases of the LSM porous layer in contact with the AISI 441 interconnect (the LSM "top" surface as shown in Fig. 2(a)) after the interconnect is removed (Fig. 6). Before the thermal treatment, the LSM air electrode shows pure perovskite phase. After the thermal treatment at 800 °C for 500 h in dry and moisture air, some minor new phases are indentified. They are $Mn_{1.5}Cr_{1.5}O_4$ and $SrMn_3O_{6-x}$. The main LSM phase maintains and all the other phases show very weak peak intensities, which mean the new compounds formed during the thermal treatment are of small amounts. It should be noticed that the YSZ phase shown in some of the XRD patterns is from the electrolyte, which is not considered in the phase analysis of the LSM layer.

For the LSM sample thermally treated in dry air, only $Mn_{1.5}Cr_{1.5}O_4$ is indentified. For the samples thermally treated in the moist air (10 vol% and 25 vol% moisture), both $Mn_{1.5}Cr_{1.5}O_4$ and $SrMn_3O_{6-x}$ are detected. $Mn_{1.5}Cr_{1.5}O_4$ formation is due to the surface deposition of the volatile Cr species and the interaction on the LSM surface. For the samples thermally treated in 10 vol% and 25 vol% moisture air, the formation of $SrMn_3O_{6-x}$ should be caused by the Sr surface segregation [37], as indicated by the XPS

results in Fig. 5. This result means that the Sr surface segregation is more significant in the wet air atmosphere. However, the amount of $SrMn_3O_{6-x}$ is too small to be compared between the 10 vol% and 25 vol% moisture conditions.

4. Discussion

4.1. LSM grain growth and sintering

From the SEM images, the microstructure of the porous LSM air electrode changes during the thermal treatment. For the as-sintered samples, the LSM particles bond with each other, forming a homogeneous network structure. During the thermal treatment at 800 °C, the grain growth and bonding continue. The LSM grains grow and bond more extensively for the sample treated in dry air, while the extent is less for the samples treated in moist air, even though the sample treated in 25 vol% moisture air exhibits more sintering than the 10 vol% moisture air sample. This means that the LSM sintering is likely to be suppressed by the water vapor in the atmosphere. Also, the atmosphere has no significant influence on the surface composition of the LSM grains. The increase in the contact between the LSM grains in the porous layer after the thermal treatment should be beneficial for reducing the ohmic resistance [15]. However, the polarization increase is generally much larger than the ohmic resistance decrease and the microstructure effects have not been well established [13,39,40]. There is more work needed to correlate the microstructure with the cell performance. On the other hand, at the LSM/AISI 441 interface, the microstructure of the LSM is the same as that across the LSM porous layer. This means that the thermal treatment temperature of 800 °C is not high enough to lead to extensive morphological changes between the LSM and the AISI 441.

4.2. Interfacial behaviors of the cell components

The LSM air electrode porous layer is in direct contact with two other cell components: the YSZ electrolyte and the AISI 441 interconnect, during the thermal treatment. For the YSZ/LSM interface, bonding forms during the sintering at 1100 °C. The bonding spot size enlarges after being treated in dry air but stays about the same after being treated in the moist atmospheres, which is consistent with the grain growth (Figs. 2 and 3). This result can be explained as the atmosphere influence on the diffusion during the thermal treatment. Dry atmosphere likely facilitates the diffusion and bonding between the LSM grains while the moist atmosphere induces the formation of substantially higher amount(s) of volatile Cr species, which suppress the diffusion of other elements such as La and Mn. Mn deposition at the YSZ surface is much less than that of La, and is further inhibited in the moist atmospheres. Cr shows significant enrichment at the YSZ/LSM interface in different atmospheres. More detailed elemental analysis should help to understand the YSZ/LSM interface interaction process.

Small particles appear on the YSZ surface after being thermally treated in moist air and the size and number of the particles are larger for the higher moisture condition (Fig. 3). Both EDS spot analysis and XPS surface analysis show that La compounds form on the YSZ surface at the as-sintered state and after the thermal treatment. Similar microstructure change has been observed in Nielsen et al. and Hagen et al.'s work [30,41]. Nielsen et al. observed small particles on the YSZ surface when the cell was treated in moist atmosphere; while the YSZ surface was clean when thermally treated in dry air [30]. Hagen et al. proposed that the microstructure change is attributed by the enhanced diffusion of Mn and the impurity elements such as Si, Ca, and S [41]. In our elemental analysis, no impurity elements are detected and La is considered the major component to cause the particle-like feature on the YSZ surface. The EDS spot analysis has a better lateral resolution of a few μm^2; the XPS, on the other hand, shows the average composition in tens of nanometers depth on the surface. For both the EDS and XPS analyses on the YSZ surface, Zr and Y are still the dominant elements and La is less than 1% from the EDS and less than 10% from the XPS, respectively (the La atomic percent at the YSZ/LSM interface in Fig. 5 is the value after excluding Zr and Y). Additionally, the quantitative result of the surface concentration of La does not show significant difference caused by the atmosphere. La is concentrated on the YSZ surface. Combining the EDS and XPS results, the particles are likely La-containing species such as $La_2Zr_2O_7$ [18,42].

At the LSM surface, the deposition of Cr is considerable for all the three samples, but there are no visible Cr-containing particles. It is believed that the Cr-containing phases form a thin layer at the LSM surface. The surface chemistry is critical to the electrochemical reaction in the air electrode; however, the surface reaction mechanism has not been well-established [43,44]. Detailed investigation of the air electrode surface reactions involving Cr deposition will be needed to improve the understanding. On the other hand, it is believed that the TPBs are the major area to determine the performance of the porous LSM air electrode; and Cr deposition can block the TPB area, causing cell performance degradation [45]. In our work, the different atmospheres cause variable YSZ/LSM interfacial bonding; the stronger bonding in dry air should be beneficial for increasing the active sites (TPB length) and reducing the ohmic resistance of the interface. However, there is no evidence that the Cr deposition at the YSZ/LSM interface is related to the TPB area.

4.3. Elemental diffusion and distribution

The distribution of La, Sr, and Mn across the LSM layer is fairly uniform except for at the YSZ/LSM interface. For the Cr, the amount decreases from the right side, where the Cr source from the AISI 441 interconnect is located, to the left side, which is further away from the AISI 441 interconnect. The surface deposition of Cr is considerable. However, it does not cause a significant difference in the LSM surface composition across the LSM porous layer. There is no visible morphological change at the LSM grain surface for all the thermal treatment conditions (Figs. 2 and 3). $Mn_{1.5}Cr_{1.5}O_4$ and $SrMn_3O_{6-x}$ phases are detected by XRD. Cr also deposits on the YSZ surface. $(Cr,Mn)_3O_4$ spinel is generally believed as the phase [46,47]. Current density can significantly accelerate this process [48] and will be reported in the future work. In the present work, no visible Cr-containing particles are found and the Cr deposition amount is small. This could be due to: (i) without polarization the driving force for Cr deposition at TPBs is not strong enough; (ii) the AISI 441 is designed to form a Mn–Cr spinel protection layer on its own surface to inhibit the release of the volatile Cr species.

At 800 °C, the volatile Cr species are affected by the water vapor in air. In moist air, the amount of the volatile $CrO_2(OH)_2$ phase is higher than the CrO_3 amount [29]. In this study, the Cr content is slightly higher for the moist air conditions after the thermal treatment. This reflects the moisture effect. However, the deposition process without current is slow in both dry and moist atmospheres, and the deposition amount is small.

5. Conclusions

The YSZ/LSM/AISI 441 tri-layer is thermally treated at 800 °C for 500 h to investigate the interaction between different SOC components in dry air, 10 vol% moisture air, and 25 vol% moisture air. The LSM microstructure shows more grain growth and bonding in dry air than in the moist atmospheres. The bonding between the YSZ and the LSM is more extensive as the moisture content

increases. At the YSZ/LSM interface, moisture leads to La-containing particle formation on the YSZ surface. Higher moisture leads to more extensive particle formation and Mn depletion at the YSZ surface. Cr deposition is detected across the porous LSM layer where the deposition amount decreases from the AISI 441 side to the YSZ side and shows accumulation at the YSZ/LSM interface. The Cr deposition amount is slightly higher for the samples thermally treated in the moist atmospheres. A small amount of $Cr_{1.5}Mn_{1.5}O_4$ is detected on the LSM surface for all the samples, and $SrMn_3O_{6-x}$ is identified for the samples thermally treated in the moist atmospheres.

Acknowledgements

Financial support from Office of Naval Research under award number N00014-11-1-0266 is sincerely acknowledged. We thank ATI Allegheny Ludlum, Brackenrigde, PA for providing the AISI 441 alloy sample.

References

[1] N.Q. Minh, J. Am. Ceram. Soc. 76 (1993) 563–588.
[2] N.P. Brandon, S. Skinner, B.C.H. Steele, Ann. Rev. Mater. Res. 33 (2003) 183–213.
[3] S.H. Jensen, P.H. Larsen, M. Mogensen, Int. J. Hydrogen Energy 32 (2007) 3253–3257.
[4] M. Ni, M.K.H. Leung, D.Y.C. Leung, Int. J. Hydrogen Energy 33 (2008) 2337–2354.
[5] A. Hauch, S.D. Ebbesen, S.H. Jensen, M. Mogensen, J. Mater. Chem. 18 (2008) 2331–2340.
[6] J.W. Fergus, Mater. Sci. Eng. A 397 (2005) 271–283.
[7] Z.G. Yang, Int. Mater. Rev. 53 (2008) 39–54.
[8] J.W. Wu, X.B. Liu, J. Mater. Sci. Technol. 26 (2010) 293–305.
[9] S.P. Simner, J.F. Bonnett, N.L. Canfield, K.D. Meinhardt, J.P. Shelton, V.L. Sprenkle, J.W. Stevenson, J. Power Sources 113 (2003) 1–10.
[10] V.A.C. Haanappel, V. Shemet, S.M. Gross, T. Koppitz, N.H. Menzler, M. Zahid, W.J. Quadakkers, J. Power Sources 141 (2005) 216–226.
[11] S.P. Jiang, J. Mater. Sci. 43 (2008) 6799–6833.
[12] S.B. Adler, Chem. Rev. 104 (2004) 4791–4843.
[13] J. Fleig, Ann. Rev. Mater. Res. 33 (2003) 361–382.
[14] M.A. Laguna-Bercero, J.A. Kilner, S.J. Skinner, Chem. Mater. 22 (2010) 1134–1141.
[15] K. Sasaki, J.P. Wurth, R. Gschwend, M. Godickemeier, L.J. Gauckler, J. Electrochem. Soc. 143 (1996) 530–543.
[16] M.J. Jorgensen, S. Primdahl, C. Bagger, M. Mogensen, Solid State Ionics 139 (2001) 1–11.
[17] S.P. Jiang, W. Wang, Solid State Ionics 176 (2005) 1185–1191.
[18] A. Mitterdorfer, L.J. Gauckler, Solid State Ionics 111 (1998) 185–218.
[19] E.V. Tsipis, V.V. Kharton, J. Solid State Electrochem. 12 (2008) 1367–1391.
[20] C. Levy, Y. Zhong, C. Morel, S. Marlin, J. Electrochem. Soc. 157 (2010) B1597–B1601.
[21] S. Taniguchi, M. Kadowaki, H. Kawamura, T. Yasuo, Y. Akiyama, Y. Miyake, T. Saitoh, J. Power Sources 55 (1995) 73–79.
[22] S.P.S. Badwal, R. Deller, K. Foger, Y. Ramprakash, J.P. Zhang, Solid State Ionics 99 (1997) 297–310.
[23] Y. Matsuzaki, I. Yasuda, Solid State Ionics 132 (2000) 271–278.
[24] S.P. Jiang, J.G. Love, Solid State Ionics 138 (2001) 183–190.
[25] S.P. Simner, M.D. Anderson, G.G. Xia, Z. Yang, L.R. Pederson, J.W. Stevenson, J. Electrochem. Soc. 152 (2005) A740–A745.
[26] L.G.J. de Haart, J. Mougin, O. Posdziech, J. Kiviaho, N.H. Menzler, Fuel Cells 9 (2009) 794–804.
[27] T. Horita, Y.P. Xiong, H. Kishimoto, K. Yamaji, M.E. Brito, H. Yokokawa, J. Electrochem. Soc. 157 (2010) B614–B620.
[28] K. Hilpert, D. Das, M. Miller, D.H. Peck, R. Weiss, J. Electrochem. Soc. 143 (1996) 3642–3647.
[29] E.J. Opila, D.L. Myers, N.S. Jacobson, I.M.B. Nielsen, D.F. Johnson, J.K. Olminsky, M.D. Allendorf, J. Phys. Chem. A 111 (2007) 1971–1980.
[30] J. Nielsen, A. Hagen, Y.L. Liu, Solid State Ionics 181 (2010) 517–524.
[31] S.H. Kim, K.B. Shim, C.S. Kim, J.T. Chou, T. Oshima, Y. Shiratori, K. Ito, K. Sasaki, J. Fuel Cell Sci. Technol. 7 (2010), 021011-1-6.
[32] Z.G. Yang, G.G. Xia, C.M. Wang, Z.M. Nie, J. Templeton, J.W. Stevenson, P. Singh, J. Power Sources 183 (2008) 660–667.
[33] A. Srisrual, S. Coindeau, A. Galerie, J.P. Petit, Y. Wouters, Corrosion Sci. 51 (2009) 562–568.
[34] M.K. Mahapatra, K. Lu, J. Am. Ceram. Soc. 94 (2011) 875–885.
[35] A. Hammouche, E. Siebert, A. Hammou, Mater. Res. Bull. 24 (1989) 367–380.
[36] T. Jin, K. Lu, Int. J. Hydrogen Energy 36 (2011) 4440–4448.
[37] T. Jin, K. Lu, J. Power Sources 196 (2011) 8331–8339.
[38] C. Brugnoni, U. Ducati, M. Scagliotti, Solid State Ionics 76 (1995) 177–182.
[39] S.P. Jiang, J.G. Love, Solid State Ionics 158 (2003) 45–53.
[40] P.R. Shearing, D.J.L. Brett, N.P. Brandon, Int. Mater. Rev. 55 (2010) 347–363.
[41] A. Hagen, K. Neufeld, Y.L. Liu, J. Electrochem. Soc. 157 (2010) B1343–B1348.
[42] M. Chen, Y.L. Liu, A. Hagen, P.V. Hendriksen, F.W. Poulsen, Fuel Cells 9 (2009) 833–840.
[43] T. Horita, K. Yamaji, M. Ishikawa, N. Sakai, H. Yokokawa, T. Kawada, T. Kato, J. Electrochem. Soc. 145 (1998) 3196–3202.
[44] G.J. la O., R.F. Savinell, Y. Shao-Horn, J. Electrochem. Soc. 156 (2009) B771–B781.
[45] E. Konysheva, H. Penkalla, E. Wessel, J. Mertens, U. Seeling, L. Singheiser, K. Hilpert, J. Electrochem. Soc. 153 (2006) A765–A773.
[46] S.P. Jiang, S. Zhang, Y.D. Zhen, J. Mater. Res. 20 (2005) 747–758.
[47] S. Wang, T.A. Cruse, M. Krumpelt, B.J. Ingram, P.A. Salvador, J. Electrochem. Soc. 158 (2011) B152–B158.
[48] M. Krumpelt, T.A. Cruse, B.J. Ingram, J.L. Routbort, S.L. Wang, P.A. Salvador, G. Chen, J. Electrochem. Soc. 157 (2010) B228–B233.